Ballistic thermoelectric properties of monolayer semiconducting transition metal dichalcogenides and oxides

G. Özbal ⓘ,[1] R. T. Senger,[1,2] C. Sevik,[3] and H. Sevinçli[4,*]

[1]*Department of Physics, Izmir Institute of Technology, 35430 Izmir, Turkey*
[2]*ICTP-ECAR Eurasian Center for Advanced Research, Izmir Institute of Technology, 35430 Izmir, Turkey*
[3]*Department of Mechanical Engineering, Faculty of Engineering, Eskişehir Technical University, Eskişehir, TR 26555, Turkey*
[4]*Department of Materials Science and Engineering, Izmir Institute of Technology, 35430 Izmir, Turkey*

Combining first-principles calculations with Landauer-Büttiker formalism, ballistic thermoelectric transport properties of semiconducting two-dimensional transition metal dichalcogenides (TMDs) and oxides (TMOs) (namely MX_2 with M = Cr, Mo, W, Ti, Zr, Hf; X = O, S, Se, Te) are investigated in their 2H and 1T phases. Having computed structural, as well as ballistic electronic and phononic transport properties for all structures, we report the thermoelectric properties of the semiconducting ones. We find that 2H phases of four of the studied structures have very promising thermoelectric properties, unlike their 1T phases. The maximum room temperature p-type thermoelectric figure of merit (ZT) of 1.57 is obtained for 2H-HfSe$_2$, which can be as high as 3.30 at $T = 800$ K. Additionally, 2H-ZrSe$_2$, 2H-ZrTe$_2$, and 2H-HfS$_2$ have considerable ZT values (both n- and p-type), that are above 1 at room temperature. The 1T phases of Zr and Hf-based oxides possess relatively high power factors, however their high lattice thermal conductance values limit their ZT values to below 1 at room temperature.

I. INTRODUCTION

Thermoelectric (TE) materials make it possible to drive electric currents using temperature gradients, and conversely cooling of a system just by using a voltage difference, namely the Seebeck and Peltier effects, respectively. The performance of TE conversion is quantified by the dimensionless figure of merit ZT, which includes strongly interrelated electronic and thermal transport properties. Because of this interrelation among Seebeck coefficient (S), electrical conductance (G), and thermal conductance (κ), significant enhancement of ZT is an extremely difficult task. Therefore improvement of TE efficiency has been relatively slow, and typical ZT values do not exceed 1 for bulk materials [1]. With the advances in the production of low-dimensional structures, a new quest for high performance TE materials gained acceleration [2–7]. The advent of atomically thin graphene provided a new platform to study transport and thermoelectric properties in two and one dimensions (2D and 1D) [8–10]. However, the absence of an electronic band gap in 2D graphene and ultrahigh thermal conductivity suppress its thermoelectric efficiency [11–15]. Still, there are numerous proposals to enhance the TE performance of graphene [9,16–26]. A more recent family of 2D materials, semiconducting TMDs and TMOs attracted attention due to the wide range of band gaps and lower lattice thermal conductivities. One of the most detailed studies on stability, electronic, mechanical, and magnetic analysis of single layer TMDs and TMOs belongs to Ataca *et al.* [27]. The majority of the theoretical studies have been devoted towards

MX_2 (M=Mo,W; X=S,Se) monolayers [28–36], few layers [37–42], hybrid nanoribbons [43,44], or heterostructures [45]. Phonon engineering [46], band structure engineering [47], and strain engineering [48–52] approaches were also employed extensively with the aim of improving thermoelectric performance of MX_2 structures. In addition to Mo and W based compounds, there are also a few studies Zr and Hf based TMDs in their 1T phases [53–57]. However, a comprehensive study on thermoelectric properties of pristine TMD/TMOs, specifically the 2H phase of Ti, Zr, and Hf based structures, is still lacking. Here, we focus on expanding the library of 2D TMD/TMO candidates starting with an investigation of their ballistic properties. Electronic transport, thermal transport, and thermoelectric properties of 26 dynamically stable semiconducting TMDs/TMOs are explored. Structural parameters are computed for obtaining accurate electronic band structures and vibrational spectra based on *ab initio* calculations. Thermoelectric coefficients are computed by combining first-principles calculations and Landauer-Büttiker formalism. Also band gap corrections are performed using hybrid HSE06 functionals when necessary.

II. METHODS

The geometrical optimization and electronic structure calculations are performed using density functional theory (DFT) using plane-wave basis sets [58] by employing projector augmented wave (PAW) potentials [59]. The exchange-correlation potential has been approximated by generalized gradient approximation (GGA) using Perdew-Burke-Ernzerhof (PBE) functionals [60]. The plane-wave cutoff energies are found to be in the range from 250 to 500 eV with

*haldunsevincli@iyte.edu.tr

convergence tests for each structure. The irreducible Brillouin zone is sampled using the Monkhorst-Pack scheme with grid sizes of $n \times n \times 1$ ($n = 5$–15) according to the convergence tests [61]. The convergence thresholds for ionic and electronic relaxations are set to 10^{-3} eV/Å and 10^{-6} eV, respectively. During the geometry optimization process, cell shape and volume are preserved. The vacuum spacing is set to 15 Å to avoid any spurious interactions between layers. In order to correct the band gap values Heyd-Scuseria-Ernzerhof (HSE06) [62] hybrid functionals are used for selected five MX$_2$ structures, where 0.25 exact Hartree-Fock and 0.75 PBE exchange mixing and the screening parameter of 0.2 Å^{-1} are used. The calculations are performed non-spin-polarized and spin-orbit interactions are not taken into consideration. The interatomic force constants (IFCs) are obtained by employing density functional perturbation theory (DFPT) [63]. Phonon band structure and heat capacity calculations are performed by using the PHONOPY package [64].

The cohesive energy (E$_c$) per atom is computed as

$$E_{\text{coh}} = (n_X E_X + n_M E_M - E_{MX_2})/(n_X + n_M). \quad (1)$$

Here, $n_{X(M)}$ denotes the number of chalcogen (transition metal) atoms in the unit cell. $E_{X(M)}$ is the energy of the isolated single atoms, and E_{MX_2} is the total energy of the MX$_2$ monolayer. In order to gain an understanding on bond characteristics, charge transfer calculations are conducted by using the Bader method [65]. The percent ionic character (%IC) of metal and chalcogen/oxygen atoms can be calculated roughly as [66]

$$\%IC = \{1 - \exp[-0.25(X_A - X_B)^2]\} \times 100 \quad (2)$$

where X_A and X_B are electronegativities of the constituent atoms.

Electronic transmission spectrum is given by the number of transmission channels in the ballistic limit. Since each studied structure exhibits hexagonal symmetry, their transmission spectra are isotropic. Therefore both transmission spectra and thermoelectric coefficients are given along one direction. Dense k-point meshes $200 \times 200 \times 1$ and $100 \times 100 \times 1$ are used in calculating transmission spectra using PBE and HSE06 functionals, respectively.

Derivation of the electronic coefficients is performed by using [67,68]

$$L_n(\mu, T) = -\frac{2}{h} \int dE \, \tau_{el}(E)(E - \mu)^n \frac{\partial f_{\text{FD}}(E, \mu, T)}{\partial E}, \quad (3)$$

with n being an integer, $\tau_{el}(E)$ the electronic transmission spectrum, and $f_{\text{FD}}(E, \mu, T)$ the Fermi-Dirac distribution function at temperature T and chemical potential μ. Using L_n, one can express the electrical conductance (G), Seebeck coefficient (S), and the electrical part of the thermal conductance (κ_{el}) as $G = e^2 L_0$, $S = (L_1/L_0)/eT$, and $\kappa_{el} = (L_2 - L_1^2/L_0)/T$, respectively.

Phonon thermal conductance is calculated using Landauer formalism [69,70],

$$\kappa_{\text{ph}} = \frac{1}{2\pi} \int d\omega \, \hbar\omega \, \tau_{ph}(\omega) \frac{\partial f_{\text{BE}}(\omega, T)}{\partial T}, \quad (4)$$

where ω is the vibrational frequency, f_{BE} stands for Bose-Einstein distribution function, and $\tau_{ph}(\omega)$ is the phonon
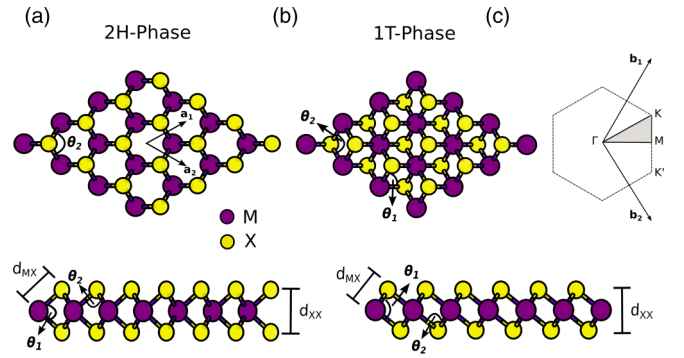

FIG. 1. Crystal structures of TMDs and TMOs. The 2H phase (a) and the 1T phase (b). The Brillouin zone, reciprocal lattice vectors, and the high symmetry points are given in (c).

transmission spectrum obtained from counting phonon modes with an average of 200 q points in the transverse direction. After computing the electronic and phononic contributions to the transport, the dimensionless thermoelectric figure of merit is obtained using

$$ZT = S^2 G T / (\kappa_{\text{el}} + \kappa_{\text{ph}}). \quad (5)$$

III. STRUCTURAL AND ELECTRONIC PROPERTIES

MX$_2$ monolayers consist of three atomic layers in the sequence of X-M-X. These sublayers are arranged in the well-known two phases (polymorphs): trigonal prismatic 2H which is a member of $P\bar{6}m2$ (D_{3h}) symmetry group and octahedral 1T which belongs to the $P\bar{3}m1$ (D_{3d}). Schematic representation of 2H and 1T phases from top and side views are shown in Figs. 1(a) and 1(b), respectively, and their first Brillouin zone is given in Fig. 1(c).

We first perform geometry optimizations and check the dynamical stabilities of the TMD/TMO monolayers by checking whether all vibrational frequencies are real and positive. While all 2H structures group-VIB (Cr, Mo, W) TMDs/TMOs are dynamically stable semiconductors, their 1T phases are unstable. Their distorted 1T$_d$ phases are dynamically stable, but all are metallic and therefore they are not within the scope of this study. On the other hand, both 2H and 1T phases of group IVB (Ti, Zr, Hf) TMDs/TMOs are dynamically stable and semiconducting. The structural parameters which determine the geometry are tabulated in Table I. The obtained parameters are in good agreement with the literature [71].

For a given phase, d_{MX} increases with increasing a. However, different phases (2H and 1T) of a given MX$_2$ (ZrSe$_2$, HfS$_2$, and HfSe$_2$) follow an opposite trend. For example, the 1T phase of ZrSe$_2$ has larger a than its 2H phase but smaller d_{MX} and h. For these structures, a is always larger for the 1T phase, whereas d_{MX} is reduced by $\sim$0.7% and h is reduced by $\sim$6–7%. Bond angles θ_1 and θ_2 follow opposite trends. Comparing two MX$_2$ structures, one observes that the structure with larger θ_1 has smaller θ_2. Also θ_1 of the 1T phase of a given structure is always larger than that in the 2H phase.

For compounds of the same phase, E_{coh} decreases with increasing a as expected. A comparison of 2H and 1T phases of the same TMD reveal that E_{coh} is always larger for the 1T

TABLE I. Structural and electronic properties of semiconducting TMDs and TMOs, which are dynamically stable. The lattice parameter of the unit cell (a), bond lengths (d_{MX}), layer heights (h), bond angles (θ_1, θ_2), band gap (E_g^{PBE}), cohesive energy (E_{coh}), transferred charge to X (ρ_M), charge received by X (ρ_X), and the fractional ionic character (FIC), respectively. Bond lengths and angles are shown in Fig. 1 and electronic band structures are illustrated in Fig. S2 [93].

MX_2	Phase	a (Å)	d_{MX} (Å)	h (Å)	θ_1 (deg)	θ_2 (deg)	E_g^{PBE} (eV)	E_{coh} (eV/atom)	ρ_M (e^-)	ρ_X (e^-)	FIC (%)
CrO_2	2H	2.63	1.91	2.32	74.77	86.96	0.37	5.34	1.48	−0.74	54.51
CrS_2	2H	3.04	2.29	2.94	79.82	83.26	0.93	4.17	1.00	−0.50	19.07
$CrSe_2$	2H	3.21	2.43	3.14	80.59	82.68	0.75	3.64	0.81	−0.41	17.97
$CrTe_2$	2H	3.48	2.64	3.41	80.63	82.66	0.53	3.09	0.56	−0.28	4.73
MoO_2	2H	2.83	2.05	2.47	74.18	87.39	0.91	6.24	1.67	−0.84	33.61
MoS_2	2H	3.18	2.41	3.13	80.77	82.55	1.67	5.14	1.07	−0.57	4.31
$MoSe_2$	2H	3.32	2.54	3.34	82.12	81.54	1.44	4.60	0.83	−0.42	3.73
$MoTe_2$	2H	3.55	2.73	3.61	82.74	81.07	1.08	4.04	0.52	−0.26	0.09
WO_2	2H	2.83	2.05	2.48	74.34	87.27	1.36	7.02	1.83	0.92	25.29
WS_2	2H	3.19	2.42	3.14	80.87	82.47	1.79	5.80	1.21	−0.61	1.20
WSe_2	2H	3.32	2.55	3.35	82.44	81.30	1.54	5.19	0.92	−0.46	0.90
WTe_2	2H	3.55	2.74	3.62	82.89	80.96	1.06	4.54	0.58	−0.29	1.68
TiS_2	2H	3.34	2.45	3.02	75.99	86.07	0.73	5.17	1.49	−0.75	23.69
$TiSe_2$	2H	3.49	2.58	3.24	77.61	84.89	0.60	4.68	1.39	−0.70	22.51
$TiTe_2$	2H	3.74	2.80	3.57	79.28	83.66	0.19	4.12	1.23	−0.61	7.54
ZrO_2	1T	3.28	2.12	1.93	79.05	100.95	4.44	7.71	2.54	−1.27	67.14
ZrS_2	1T	3.69	2.57	2.90	88.59	91.41	1.20	5.89	2.05	−1.02	32.34
$ZrSe_2$	2H	3.71	2.73	3.38	76.61	85.62	0.79	5.21	1.80	−0.90	31.07
	1T	3.80	2.71	3.17	90.73	89.27	0.51	5.35	1.87	−0.94	31.07
$ZrTe_2$	2H	3.93	2.94	3.73	78.83	83.99	0.45	4.62	1.58	−0.79	13.78
HfO_2	1T	3.24	2.11	1.93	79.38	100.62	4.87	7.90	2.32	−1.16	68.17
HfS_2	2H	3.53	2.57	3.13	74.92	86.85	1.09	5.78	1.84	−0.92	33.61
	1T	3.64	2.55	2.89	88.90	91.11	1.29	6.00	1.91	−0.95	33.61
$HfSe_2$	2H	3.67	2.70	3.36	76.78	85.50	0.88	5.25	1.68	−0.84	32.34
	1T	3.76	2.68	3.14	90.92	89.08	0.60	5.42	1.76	−0.88	32.34
$HfTe_2$	2H	3.90	2.91	3.69	78.63	84.14	0.36	4.61	1.48	−0.74	14.79

phase. That is to say, 1T phases of studied Zr and Hf based compounds are energetically more stable, in agreement with previous studies [72–76]. According to Table I, TMOs exhibit the highest ionic character in general, which is because of the largest charge transfer between the transition metal and the oxygen atoms. 1T-HfO_2, which has the highest cohesive energy and the widest electronic band gap shows the highest ionic character, whereas 2H-$MoTe_2$ possesses fractional covalent character.

Electronic band diagrams of the investigated structures are plotted in the Supplemental Material (see Fig. S2) [93]. The 2H phases of group-VIB dichalcogenides are direct band gap semiconductors, whereas their oxides have indirect band gaps. Group-IVB dichalcogenides and oxides are all indirect semiconductors. Electronic band gaps ranging between 0.19 eV and 4.87 eV are obtained with PBE functionals. HSE06 calculations are performed for materials which have a E_g^{PBE} less than 0.5 eV. This is because the main effect of the hybrid functional to the band structure is to increase the band gap with changing the band dispersions only slightly. When the band gap of a structure is less than $10k_BT$, simultaneous contribution from the holes in the valence band and electrons in the conduction band suppresses the Seebeck coefficient [77–81]. The effect of hybrid functionals on electronic transport and thermoelectric properties will be discussed in more detail

later. The electronic band diagrams of 2H-CrO_2, 2H-$TiTe_2$, 2H-$ZrTe_2$, and 2H-$HfTe_2$ within PBE+HSE06 functionals are presented in Fig. 2. Band gap values are increased to 0.90, 0.97, 1.05, and 0.93 eV for CrO_2, $TiTe_2$, $ZrTe_2$, and $HfTe_2$, respectively.

IV. VIBRATIONAL PROPERTIES

It is necessary to check whether imaginary or negative frequencies exist in phonon dispersions to check the dynamical stabilities of the structures. We note that dynamical stability is a necessary condition but not conclusive for experimental realization. When both 2H and 1T phases of MX_2 monolayers are considered, 30 structures are found to be dynamically stable. Four of these structures are excluded in this study as they are either metallic or semi-metallic. Phonon spectra of the remaining 26 structures are given in the Supplemental Material (see Fig. S1) [93]. A cautionary note is in order here. Smearing is a computational tool that smoothens the Fermi distribution function around the Fermi energy. It is a necessary ingredient in DFT calculations. Even graphene can be found dynamically unstable if appropriate smearing is not used. There does not exist a recipe for determining the smearing method or value. There are a few methods to implement smearing, most of them without a clear
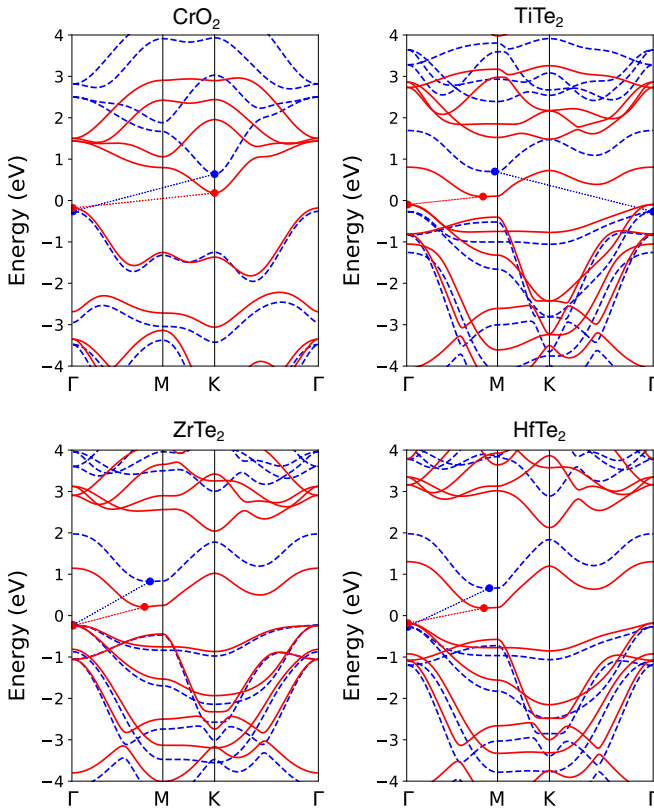
FIG. 2. Calculated electronic band structures of selected 2H-MX$_2$ compounds; CrO$_2$, TiTe$_2$, ZrTe$_2$, HfTe$_2$ based on PBE (red solid line) and PBE+HSE (blue dashed line) functional. Fermi level is set to zero for all subfigures.

TABLE II. Phonon thermal conductance values for various temperatures.

MX_2	Phase	κ_{ph} (nW/K/nm)		
		300 K	500 K	800 K
CrO$_2$	2H	2.09	2.49	2.66
CrS$_2$	2H	1.24	1.34	1.37
CrSe$_2$	2H	0.83	0.87	0.88
CrTe$_2$	2H	0.60	0.62	0.63
MoO$_2$	2H	1.63	1.89	2.00
MoS$_2$	2H	1.03	1.10	1.13
MoSe$_2$	2H	0.72	0.75	0.76
MoTe$_2$	2H	0.54	0.55	0.55
WO$_2$	2H	1.29	1.48	1.56
WS$_2$	2H	0.83	0.89	0.91
WSe$_2$	2H	0.66	0.68	0.68
WTe$_2$	2H	0.50	0.51	0.51
TiS$_2$	2H	0.95	1.00	1.02
TiSe$_2$	2H	0.95	0.99	1.00
TiTe$_2$	2H	0.70	0.72	0.73
ZrO$_2$	1T	1.45	1.71	1.81
ZrS$_2$	1T	0.83	0.87	0.89
ZrSe$_2$	2H	0.54	0.55	0.56
	1T	0.71	0.72	0.73
ZrTe$_2$	2H	0.55	0.56	0.56
HfO$_2$	1T	1.28	1.50	1.60
HfS$_2$	2H	0.65	0.67	0.68
	1T	0.71	0.74	0.75
HfSe$_2$	2H	0.51	0.51	0.52
	1T	0.59	0.61	0.61
HfTe$_2$	2H	0.48	0.49	0.49

physical meaning. Fermi-Dirac smearing, on the other hand, is interpreted as electronic temperature. Being only applied on electrons and not on ions, it should be not confused with real temperature. Still, Fermi-Dirac smearing is used to identify temperature dependent stabilization in certain cases [82–84]. In this work, we implement Fermi-Dirac smearing and scan possible smearing values systematically.

For lower values of smearing ($\sigma = 0.05$ eV) 2H-TiS$_2$, 2H-ZrSe$_2$, and 2H-HfS$_2$ out-of-plane ZA mode possess negative frequencies around the high symmetry points, whereas 2H-HfSe$_2$ has negative frequencies ony around the K point. When the smearing is increased ($\sigma = 0.4$ eV for 2H-HfSe$_2$ and $\sigma = 0.5$ eV for 2H-TiS$_2$, 2H-ZrSe$_2$, 2H-HfS$_2$) all phonons frequencies are found positive. These σ values are in the same range with those used in the literature [82,85,86].

The phonon band gap, which separates the acoustic modes from the six optical branches, decreases with decreasing mass difference between the constituent elements of MX$_2$ compounds. The acoustic bandwidths become narrower with increasing average mass, whereas all bands are pushed towards lower frequencies with increasing total mass of the compounds. In previous studies, in which phonon-phonon scattering was taken into account, the scatterings were limited when a band gap is present. Therefore the absence of a phonon band gap was found helpful to reduce lattice thermal conductivity. Conversely, in the ballistic regime, the presence of a phonon band gap reduces lattice thermal conductivity,

simply because there is no transmission within gap. Briefly, both a wide phonon band gap and reduced phonon frequencies decrease thermal conductance and enhance the TE performance. Thermal conductance of the investigated TMD/TMOs at various temperatures are listed in Table II. 2H-CrO$_2$ is composed of the lightest atoms in the group, hence has the largest phonon thermal conductance at all temperatures. As temperature increases thermal conductance of CrO$_2$ increases considerably. A similar trend appears for all the TMOs, which is associated with the relatively higher ω_{max} values, because of oxygen being the lightest element in group VIA. As will be discussed later, 2H phases of ZrSe$_2$, ZrTe$_2$, HfS$_2$, and HfSe$_2$ are found to be both n- and p-type promising thermoelectric candidates. In order to clarify influence of thermal properties on thermoelectric performance, vibrational spectra and transport properties are presented in Fig. 3, only for these four materials.

In a previous study, which investigated the thermal conductivities of 2H group-VIB TMD family by using the Boltzmann transport equation [87], it was found that the thermal conductivities of sulfides (MS$_2$) and selenides (MSe$_2$) increase as M changes from Cr to Mo, and from Mo to W, due to the rapid increase in the phonon relaxation time. In contrast to this, we find that κ_{ph} decreases as M changes from Cr to Mo to W at the ballistic limit, because of increasing atomic masses. This inverse behavior is validated with the calculation
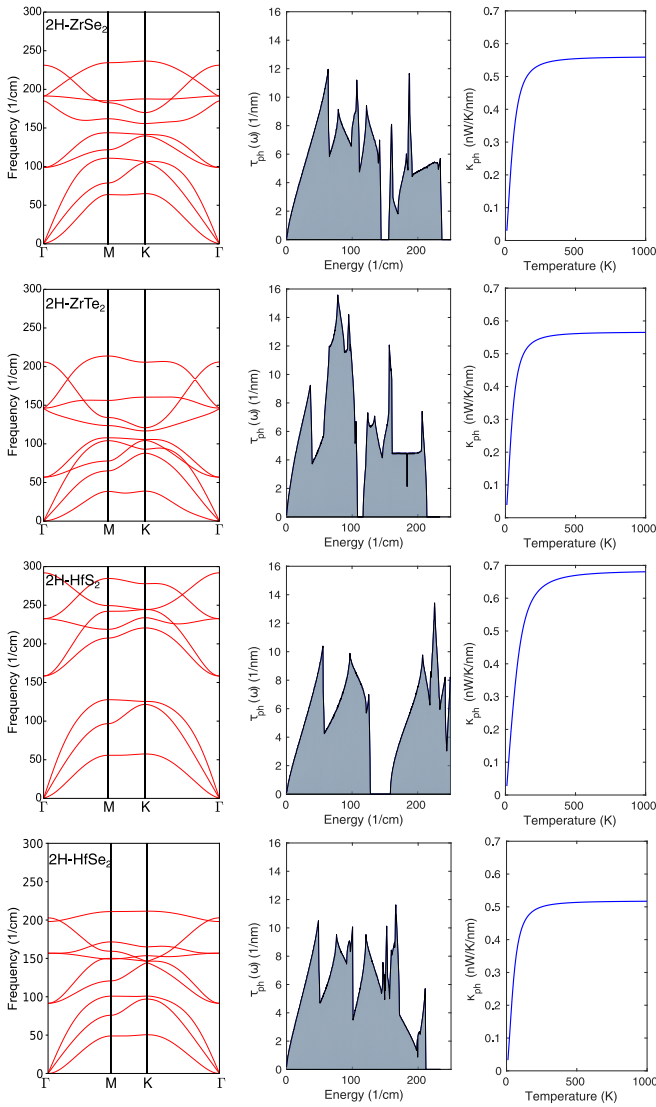
FIG. 3. Phonon dispersion relations, phonon transmission spectra, and phonon thermal conductance as a function of temperature of ZrSe$_2$, ZrTe$_2$, HfS$_2$, and HfSe$_2$ are shown, respectively.

of correlation between average atomic mass of the unit cell and phonon thermal conductance, where %80, %78, and %77 inverse correlations are found for 300 K, 500 K, and 800 K, respectively. In addition, it is found that the correlation between m and κ_{ph} does not change at even higher temperatures.

We also note that in a recent theoretical study the ballistic thermal conductance value of MoS$_2$ was reported as 1.06 nW/K for a sample having a width of 1.27 nm [88]. The corresponding thermal conductance per width value (0.84 nW K^{-1} nm^{-1}) is considerably less than our present result (1.03 nW K^{-1} nm^{-1}). The disagreement is because we employ a fine sampling of the k points in the transmission spectrum, whereas Cai *et al.* uses only the Γ point. Hence they find a stepwise transmission spectrum like in a one-dimensional system, which overestimates the contributions from low energies.
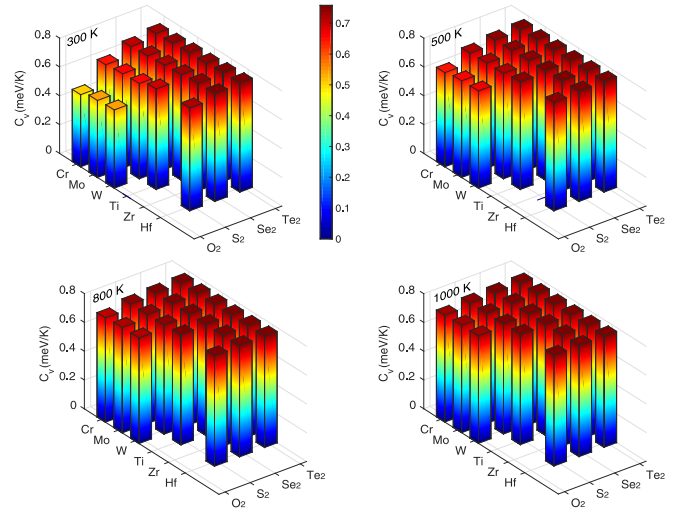

FIG. 4. Heat capacities at various temperatures from 300 K to 1000 K are shown for the semiconducting compounds in the 2H phase.

The vibrational heat capacity at constant volume is calculated using

$$C_v = k_B \int d\omega \, \rho(\omega) \, p(\omega, T), \tag{6}$$

where ρ is the phonon density of states, $p(x) = -x^2 \partial f_{\mathrm{BE}}/\partial x$, $f_{BE} = 1/(e^x - 1)$ being the Bose-Einstein distribution function, and $x = \hbar\omega/k_B T$. In Figs. 4 and 5 the vibrational heat capacities are plotted at $T = 300$ K, 500 K, 800 K, and 1000 K. At lower temperatures, the heat capacity is dominated by low frequency modes which possess low group velocity and larger phonon density of states. Therefore, heavier compounds, like Hf and Zr based structures, have higher heat
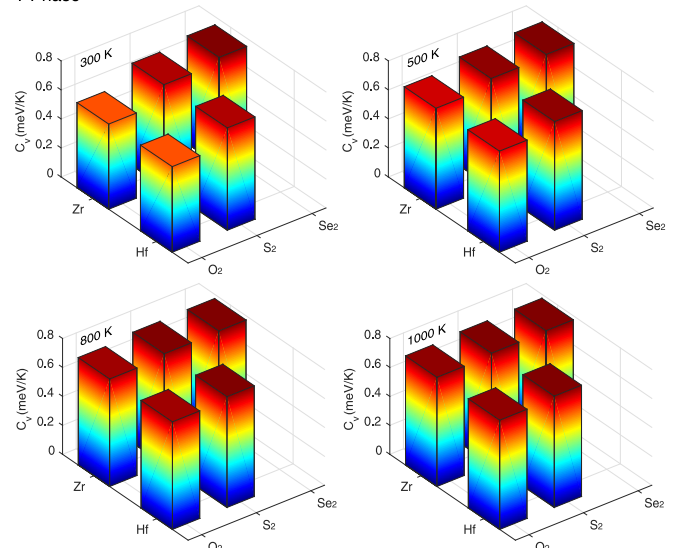

FIG. 5. Heat capacities at various temperatures from 300 K to 1000 K are shown for the semiconducting compounds in the 1T phase.

capacities at 300 K. At increased temperatures, the differences in the C_v tend to decrease. At 1000 K, the function $p(x)$ is almost constant and equal to unity in the entire spectrum. The heat capacities approach the classical limit, which is proportional to the number of modes per unit cell.

V. THERMOELECTRIC PROPERTIES

According to the Mott formula [20,89,90]

$$S(T, \mu) \approx \frac{\pi^2 k_B^2 T}{3e} \left. \frac{d \ln \tau(E)}{dE} \right|_\mu, \quad (7)$$

the logarithmic derivative of the electronic transmission determines the Seebeck coefficient at low temperatures. Namely, the abrupt changes in the transmission spectrum gives rise to large Seebeck coefficient and power factor. The structures studied in this work agree with this rule of thumb. The thermoelectric coefficients, S, P, and ZT, for various temperatures are tabulated in Table III. The chemical potential (μ) is chosen around the band edges where ZT is maximized. The difference between μ at the valence band edge (conduction band edge) and the μ where p-type ZT (n-type ZT) is maximized is crucial for determining the optimal doping levels of the semiconductor (see Table S1) [93]. One observes that most of the 2H group-VIB TMD/TMOs have relatively low ZT

values compared to the 2H group-IVB TMD/TMOs. Notably, oxide compounds from group VIB show considerably weak TE performance due to their low atomic masses and hence high κ_{ph}. While p-type ZT values of the group-VIB TMOs reach a maximum value around 0.11 at room temperature, the corresponding values for n-type ZT can be as high as 0.16. There are various theoretical studies on the TE properties of MX_2 (M = Mo,W; X = S,Se) monolayers. In a previous work, n-type ZT of the most studied MoS_2 monolayer was predicted 0.04 by using the Boltzmann equation and equilibrium molecular dynamics (EMD) simulations [33]. Wickramaratne *et al.* obtained different n-type ZT values (0.87/1.35) by adopting layer thickness dependent and constant κ_{ph} values in diffusive regime calculations. In another work, reported ZT values are overestimated compared to our findings for well-studied MoS_2, $MoSe_2$, WS_2, and WSe_2 in the frame of ballistic transport [30]. In addition, previously reported p- and n-type ZT values (0.58/0.25) in the ballistic regime are consistent with our results (0.47/0.22) [34]. Also, there is an agreement on the results of Huang *et al.* that p-type ZT of MoS_2 at room temperature and n-type ZT of WSe_2 at high temperatures are found to be higher than those of the $MoSe_2$ and WS_2 [34].

Among all investigated compounds, $ZrSe_2$, HfS_2, and $HfSe_2$ are dynamically stable in both 2H and 1T phases.

TABLE III. p- and n-type Seebeck coefficient (S), power factor (P), and thermoelectric figure of merit (ZT) at different temperatures based on PBE calculations.

MX_2	Phase	S (10^{-4} V/K)			P (10^{-3} nW/K^2nm)			ZT		
		300 K	500 K	800 K	300 K	500 K	800 K	300 K	500 K	800 K
CrO_2[a]	2H	2.01/−1.86	1.99/−1.93	1.49/−1.80	0.69/1.15	0.89/1.52	0.98/1.92	0.10/0.15	0.17/0.27	0.23/0.44
CrS_2	2H	2.04/−1.99	2.20/−2.23	2.47/−2.43	1.57/1.20	2.58/1.66	3.50/2.41	0.33/0.27	0.74/0.53	1.40/1.02
$CrSe_2$	2H	2.13/−1.97	2.35/−2.39	2.65/−2.66	1.30/1.31	1.87/1.75	2.74/2.50	0.41/0.40	0.83/0.80	1.59/1.49
$CrTe_2$	2H	2.08/−2.24	2.48/−2.40	2.46/−2.43	1.35/1.26	1.82/1.77	2.76/2.69	0.55/0.54	1.08/1.05	1.70/1.59
MoO_2	2H	1.92/−1.94	1.95/−1.97	2.02/−2.15	0.51/0.82	0.66/1.06	0.84/1.35	0.09/0.14	0.17/0.26	0.30/0.47
MoS_2	2H	2.05/−2.07	2.37/−2.13	2.52/−2.52	1.89/0.81	2.31/1.17	2.88/1.98	0.47/0.22	0.86/0.45	1.46/0.97
$MoSe_2$	2H	2.08/−2.00	2.27/−2.45	2.57/−2.79	1.02/0.95	1.38/1.68	1.95/3.17	0.38/0.35	0.74/0.81	1.38/1.91
$MoTe_2$	2H	2.18/−2.11	2.36/−2.48	2.71/−2.99	1.06/0.97	1.46/1.62	1.98/2.66	0.51/0.46	1.00/1.00	1.85/2.21
WO_2	2H	2.01/−1.88	2.01/−2.10	2.06/−2.14	0.50/0.75	0.65/0.96	0.82/1.25	0.11/0.16	0.21/0.30	0.37/0.54
WS_2	2H	2.08/−2.00	2.28/−2.12	2.58/−2.62	1.41/0.67	1.95/1.00	2.38/1.90	0.43/0.22	0.86/0.46	1.50/1.08
WSe_2	2H	2.06/−1.97	2.24/−2.43	2.51/−2.85	0.83/0.86	1.09/1.93	1.47/3.43	0.34/0.33	0.67/0.92	1.21/2.18
WTe_2	2H	1.99/−2.07	2.37/−2.33	2.59/−2.82	0.82/0.68	1.06/0.98	1.42/1.72	0.42/0.36	0.83/0.74	1.49/1.57
TiS_2	2H	2.42/−2.24	2.47/−2.61	2.52/−2.52	3.74/4.43	3.98/4.84	3.98/5.29	0.98/1.05	1.55/1.79	2.14/2.66
$TiSe_2$	2H	2.19/−2.39	2.38/−2.54	2.33/−2.39	3.33/3.43	3.68/3.99	4.31/4.64	0.86/0.90	1.38/1.51	1.81/2.09
$TiTe_2$[a]	2H	1.94/−2.16	1.26/−1.64	1.11/−1.21	1.19/2.78	1.39/3.06	2.65/2.86	0.40/0.90	0.38/0.87	0.38/0.55
ZrO_2	1T	2.20/−2.01	2.37/−2.34	2.47/−2.58	5.12/3.35	5.56/5.17	5.65/6.25	0.86/0.52	1.28/1.08	1.87/1.94
ZrS_2	1T	2.02/−2.19	2.21/−2.30	2.45/−2.69	0.67/1.85	0.88/2.40	1.31/2.78	0.23/0.57	0.44/1.04	0.87/1.75
$ZrSe_2$	2H	2.38/−2.43	2.63/−/2.76	2.75/−2.87	3.36/3.59	3.34/4.00	3.29/4.21	1.41/1.42	2.19/2.41	2.96/3.61
$ZrSe_2$	1T	1.93/−2.09	2.13/−2.40	1.90/−2.05	0.56/1.80	0.72/2.22	0.91/2.71	0.22/0.63	0.43/1.16	0.65/1.76
$ZrTe_2$[a]	2H	2.26/−2.35	2.65/−2.50	2.11/−2.02	2.56/2.82	2.84/3.21	4.10/3.85	1.06/1.18	1.73/1.88	1.58/1.67
HfO_2	1T	2.33/−2.28	2.45/−2.45	2.53/−2.63	4.80/2.67	5.28/3.92	5.43/5.30	0.92/0.54	1.38/0.99	2.00/1.80
HfS_2	2H	2.38/−2.26	2.62/−2.62	2.70/−2.83	3.85/3.33	3.78/3.59	3.59/3.88	1.38/1.17	2.11/1.89	3.03/2.92
HfS_2	1T	2.05/−2.32	2.21/−2.36	2.38/−2.71	0.66/1.87	0.85/2.39	1.16/2.69	0.26/0.67	0.50/1.19	0.92/1.96
$HfSe_2$	2H	2.55/−2.47	2.73/−2.75	2.83/−2.91	3.36/2.74	3.35/2.91	3.40/3.19	1.57/1.28	2.36/2.04	3.30/3.04
$HfSe_2$	1T	1.92/−2.20	2.13/−2.46	2.12/−2.65	0.56/1.84	0.73/2.23	0.92/2.61	0.26/0.75	0.51/1.35	0.84/2.11
$HfTe_2$[a]	2H	2.29/−2.31	2.24/−2.44	1.74/−1.86	1.05/2.41	1.52/2.64	2.48/3.09	0.56/1.17	1.00/1.75	0.91/1.34

[a]Electronic transport and thermoelectric properties are performed based on HSE06+PBE functional for these selected MX_2 compounds. p/n-type ZT values for various temperatures are listed in Table IV. In addition $\tau_{el}(E)$, S, PF, and ZT are demonstrated in Fig. S3 [93].

TABLE IV. p- and n-type ZT values at different temperatures based on the HSE06 calculations.

MX_2	Phase	ZT (p-/n-type)		
		300 K	500 K	800 K
CrO_2	2H	0.09/0.13	0.17/0.23	0.30/0.42
$TiTe_2$	2H	0.47/0.81	0.90/1.37	1.70/2.18
$ZrTe_2$	2H	0.80/1.08	1.49/1.74	2.47/2.67
$HfTe_2$	2H	0.52/1.03	1.00/1.71	1.76/2.62
TiS_2	1T	0.11/0.37	0.21/0.70	0.38/1.21

We predict substantial differences in their TE performances. Both n-type and p-type ZT values of the 2H phases are much larger than those of the 1T phase, and κ_{ph} of the 1T phases are always slightly higher than the 2H phases (see Table II). The underlying reason lies mostly in their electronic band structures. The frontier bands in the 2H phase are less dispersive than in the 1T phase. The valence band maximum is almost flat, which leads to sharp changes in the DOS and the electronic transmission spectrum and give rise to enhanced S, P, and ZT. As a result, the p-type ZT values of the 2H phases are five to six times higher than those of the 1T phases. In the n-type ZT, the difference is not as dramatic as in the p-type ZT, but those of 2H phases are considerably larger again. 1T phases of $ZrSe_2$, $HfSe_2$, and HfS_2 were previously predicted to have promising ZT values, when phonon scatterings are taken into account [53,56].

In order to quantify the role of κ_{ph} on ZT, we study their correlation from the available data. The p-type ZT for 2H compounds is inversely correlated with κ_{ph} as 55%, 60%, and 59% at 300 K, 500 K, and 800 K, respectively. On the other hand, inverse correlation between n-type ZT and κ_{ph} is slightly larger than that of p-type ZT. Inverse correlation values of 57%, 62%, and 61% are obtained for the same temperatures. These illustrate the role of κ_{ph} in determining the TE performance of the crystals considered.

The 2H phases of $ZrSe_2$, $ZrTe_2$ HfS_2, and $HfSe_2$ provide ZT values larger than 1 for both n- and p-type carriers at room temperature. The electronic transmission, Seebeck coefficient, power factor, and TE figure of merit of these compounds are presented in Fig. 6. Although 2H-$ZrSe_2$ and 2H-$ZrTe_2$ have almost the same thermal conductance values, $ZrTe_2$ has the lowest ZT compared to other promising compounds due to relatively smooth transmission spectra at the valence band edge. It is also observed that PBE results yield a decreasing ZT for $ZrTe_2$ above 500 K. This stems from the fact that the band gap of $ZrTe_2$ as predicted from PBE is not sufficient to support an efficient TE response at high temperatures. We use hybrid functionals to correct the calculated band gap, which will be discussed separately below. Abrupt changes in the transmission spectra are observed at the valence band edges of $ZrSe_2$, HfS_2, and $HfSe_2$ (see Fig. 6).

Altough κ_{ph} of 2H-$HfTe_2$ is lower than that of 2H-$HfSe_2$, its p-type ZT is much lower than that of 2H-$HfSe_2$, which is found to have the highest p-type ZT value (1.57) at room temperature. The lower ZT value of 2H-$HfTe_2$ is because of its electronic transmission being smoother than that of 2H-$HfSe_2$. In the case of n-type ZT, in addition to these
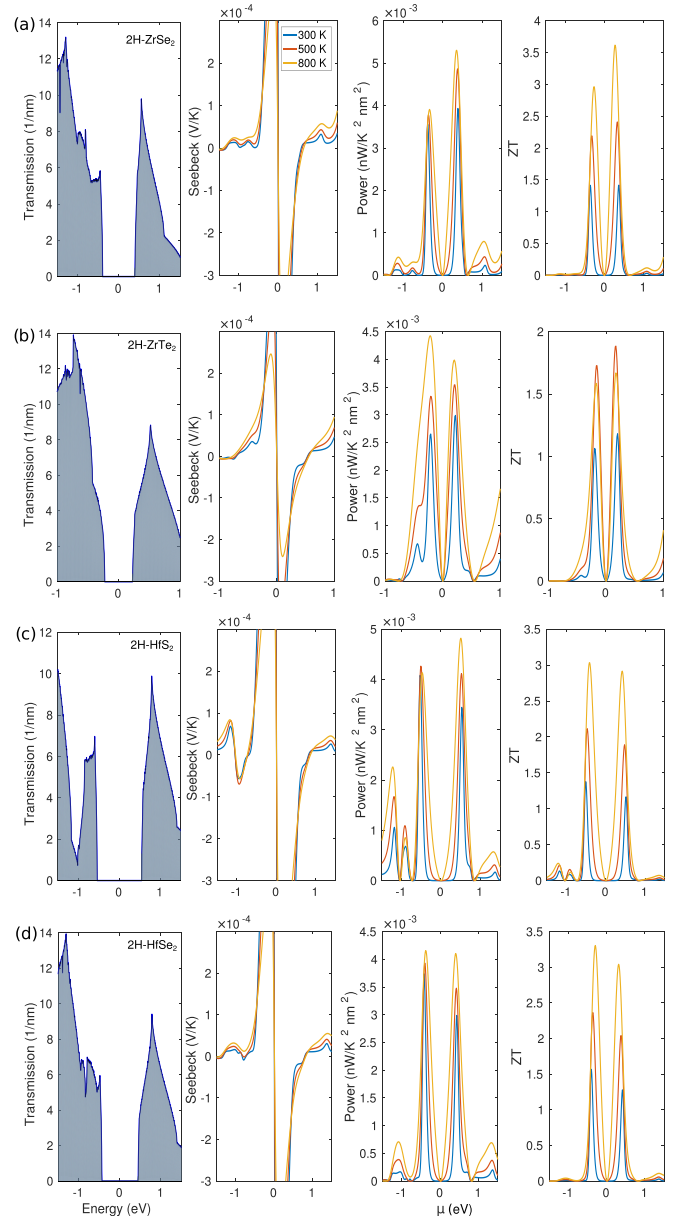

FIG. 6. Electronic transmission, Seebeck coefficient, power factor, and thermoelectric figure of merit are plotted around the Fermi level for 2H-$ZrSe_2$, 2H-$ZrTe_2$, 2H-HfS_2, and 2H-$HfSe_2$.

four TMDs, for 2H-$HfTe2$ and 2H-TiS_2, it exceeds 1 at room temperature. It is worth mentioning that a remarkably high p-type power factor is achieved for the 1T-ZrO_2 and 1T-HfO_2 but their lattice thermal conductances are higher than those of 2H-$ZrSe_2$, 2H-$ZrTe_2$, 2H-HfS_2, and 2H-$HfSe_2$ by about a factor of 2 or 3, thus their ZT values remain under 1 at 300 K. In principle, TE response of these oxides can be enhanced by reducing κ_{ph} with phonon engineering.

Seebeck coefficient is reduced with simultaneous contribution of p- and n-type carriers. Accordingly, obtaining accurate S, PF, and ZT values will mostly depend on electronic band gap of material, especially at higher temperatures. If the band gap of the material is smaller than about $10k_BT$, S is suppressed with increasing temperature as in the cases of
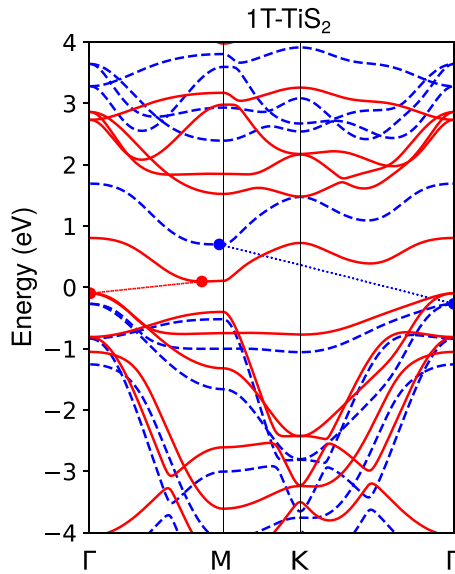
FIG. 7. Electronic band structure of 1T-TiS$_2$ with PBE (solid red) and hybrid HSE06 (dashed blue) functionals. Transition from semimetallic to semiconducting phase occurs with the hybrid functional.

2H-CrO$_2$, 2H-HfTe$_2$, 2H-TiTe$_2$, and 2H-ZrTe$_2$. The E_g^{PBE} is 0.36 eV (0.45 eV) for 2H-HfTe$_2$ (2H-ZrTe$_2$), and S is suppressed when temperature is above 300 K (500 K). Suppression of S reduces ZT when T is above 500 K for 2H-HfTe$_2$, because the increase in G compensates the decrease in S at lower temperatures. For 2H-CrO$_2$, a similar trend in S is observed, however ZT is not suppressed at higher temperatures because G increases with T. 2H-TiTe$_2$ has the narrowest E_g^{HSE} (0.19 eV) among the investigated TMDs. Therefore, the decrease in S and ZT appear above room temperature. $\tau_{el}(E)$, S, PF, and ZT calculated from hybrid-functional-corrected band gaps are demonstrated in the Supplemental Material (see Fig. S3) [93]. Band gap correction using hybrid functionals results in better ZT values for these MX_2 compounds as seen in Table IV.

Besides the semiconducting TMD/TMOs, TE properties of semimetallic 1T-TiS$_2$ is also investigated. 1T-TiS$_2$ is more stable with a E_{coh}=5.31 eV, which is higher than its 2H phase for about 0.14 eV [91]. HSE06 correction exhibits a transition from semimetallic to semiconducting behavior as shown in Fig. 7 with a band gap of 0.62 eV, in agreement with previous results [92]. It is clearly seen that 1T-TiS$_2$ does not achieve a high value of p-type ZT, but n-type ZT exceeds 1 when temperature reaches 800 K (see Table IV and Fig. S3) [93].

We note that inclusion of spin-orbit coupling (SOC) should be expected to give rise to quantitative changes in the thermoelectric coefficients of the structures. Lifting the spin degeneracy, SOC can be expected to reduce the TE efficiency for structures where the SOC is strong.

VI. CONCLUSION

We have investigated structural, electronic, vibrational, as well as ballistic transport and thermoelectric properties of a large family of TMDs/TMOs by using a combination of *ab initio* and Landauer-Büttiker formalisms. We have identified promising thermoelectric materials which possess high ZT values close to or above 1 at room temperature. In particular, high p-type and n-type TE figure of merit are found for 2H-HfSe$_2$ and 2H-ZrSe$_2$, respectively. Moreover, our calculations reveal that two TMO monolayers, 1T-ZrO$_2$ and 1T-HfO$_2$, can be promising p-type thermoelectric candidates at room temperature.

ACKNOWLEDGMENTS

[1] B. Poudel, Q. Hao, Y. Ma, Y. Lan, A. Minnich, B. Yu, X. Yan, D. Wang, A. Muto, D. Vashaee, X. Chen, J. Liu, M. S. Dresselhaus, G. Chen, and Z. Ren, Science **320**, 634 (2008).

[2] L. D. Hicks and M. S. Dresselhaus, Phys. Rev. B **47**, 12727 (1993).

[3] L. D. Hicks and M. S. Dresselhaus, Phys. Rev. B **47**, 16631 (1993).

[4] G. D. Mahan and H. B. Lyon, J. Appl. Phys. **76**, 1899 (1994).

[5] L. D. Hicks, T. C. Harman, X. Sun, and M. S. Dresselhaus, Phys. Rev. B **53**, R10493 (1996).

[6] D. A. Broido and T. L. Reinecke, Appl. Phys. Lett. **67**, 100 (1995).

[7] M. Dresselhaus, G. Chen, M. Tang, R. Yang, H. Lee, D. Wang, Z. Ren, J.-P. Fleurial, and P. Gogna, Adv. Mater. **19**, 1043 (2007).

[8] T. A. Amollo, G. T. Mola, M. S. K. Kirui, and V. O. Nyamori, Crit. Rev. Solid State Mater. Sci. **43**, 133 (2018).

[9] P. Dollfus, V. H. Nguyen, and J. Saint-Martin, J. Phys.: Condens. Matter **27**, 133204 (2015).

[10] Y. Xu, Z. Li, and W. Duan, Small **10**, 2182 (2014).

[11] Y. M. Zuev, W. Chang, and P. Kim, Phys. Rev. Lett. **102**, 096807 (2009).

[12] F. Ghahari, H.-Y. Xie, T. Taniguchi, K. Watanabe, M. S. Foster, and P. Kim, Phys. Rev. Lett. **116**, 136802 (2016).

[13] A. A. Balandin, Nat. Mater. **10**, 569 (2011).

[14] J.-W. Jiang, J.-S. Wang, and B. Li, Phys. Rev. B **79**, 205418 (2009).

[15] Z. Wang, R. Xie, C. T. Bui, D. Liu, X. Ni, B. Li, and J. T. L. Thong, Nano Lett. **11**, 113 (2011).

[16] Y. Anno, K. Takei, S. Akita, and T. Arie, Adv. Electron. Mater. **1**, 1500175 (2015).

[17] Y. Anno, Y. Imakita, K. Takei, S. Akita, and T. Arie, 2D Materials **4**, 025019 (2017).

[18] R. D'Souza and S. Mukherjee, J. Appl. Phys. **124**, 124301 (2018).

[19] D. Dragoman and M. Dragoman, Appl. Phys. Lett. **91**, 203116 (2007).

[20] T. Gunst, T. Markussen, A.-P. Jauho, and M. Brandbyge, Phys. Rev. B **84**, 155449 (2011).

[21] H. Sevinçli, C. Sevik, T. Çağin, and G. Cuniberti, Sci. Rep. **3**, 1228 (2013).

[22] H. Sevinçli and G. Cuniberti, Phys. Rev. B **81**, 113401 (2010).

[23] L. M. Sandonas, H. Sevinçli, R. Gutierrez, and G. Cuniberti, Adv. Sci. **5**, 1700365 (2018).

[24] F. Mazzamuto, V. Hung Nguyen, Y. Apertet, C. Caër, C. Chassat, J. Saint-Martin, and P. Dollfus, Phys. Rev. B **83**, 235426 (2011).

[25] Y. Ouyang and J. Guo, Appl. Phys. Lett. **94**, 263107 (2009).

[26] K. Yang, Y. Chen, R. D'Agosta, Y. Xie, J. Zhong, and A. Rubio, Phys. Rev. B **86**, 045425 (2012).

[27] C. Ataca, H. Sahin, and S. Ciraci, J. Phys. Chem. C **116**, 8983 (2012).

[28] C. Adessi, S. Thebaud, R. Bouzerar, and G. Bouzerar, J. Phys. Chem. C **121**, 12577 (2017).

[29] B. Ouyang, S. Chen, Y. Jing, T. Wei, S. Xiong, and D. Donadio, J. Materiomics **4**, 329 (2018).

[30] K.-X. Chen, X.-M. Wang, D.-C. Mo, and S.-S. Lyu, J. Phys. Chem. C **119**, 26706 (2015).

[31] H. Babaei, J. M. Khodadadi, and S. Sinha, Appl. Phys. Lett. **105**, 193901 (2014).

[32] K. Nakamura, Jpn. J. Appl. Phys. **57**, 06HE04 (2018).

[33] Z. Jin, Q. Liao, H. Fang, Z. Liu, W. Liu, Z. Ding, T. Luo, and N. Yang, Sci. Rep. **5**, 18342 (2015).

[34] W. Huang, H. Da, and G. Liang, J. Appl. Phys. **113**, 104304 (2013).

[35] G. Zhang and Y.-W. Zhang, J. Mater. Chem. C **5**, 7684 (2017).

[36] S. Kumar and U. Schwingenschlögl, Chem. Mater. **27**, 1278 (2015).

[37] A. Arab and Q. Li, Sci. Rep. **5**, 13706 (2015).

[38] D. Wickramaratne, F. Zahid, and R. K. Lake, J. Chem. Phys. **140**, 124710 (2014).

[39] M. Kayyalha, J. Maassen, M. Lundstrom, L. Shi, and Y. P. Chen, J. Appl. Phys. **120**, 134305 (2016).

[40] K. Hippalgaonkar, Y. Wang, Y. Ye, D. Y. Qiu, H. Zhu, Y. Wang, J. Moore, S. G. Louie, and X. Zhang, Phys. Rev. B **95**, 115407 (2017).

[41] W. Huang, X. Luo, C. K. Gan, S. Y. Quek, and G. Liang, Phys. Chem. Chem. Phys. **16**, 10866 (2014).

[42] R.-N. Wang, G.-Y. Dong, S.-F. Wang, G.-S. Fu, and J.-L. Wang, Phys. Chem. Chem. Phys. **19**, 5797 (2017).

[43] Y. Ouyang, Y. Xie, Z. Zhang, Q. Peng, and Y. Chen, J. Appl. Phys. **120**, 235109 (2016).

[44] Z. Zhang, Y. Xie, Q. Peng, and Y. Chen, Sci. Rep. **6**, 21639 (2016).

[45] T.-m. Wu, R.-x. Xu, X. Zheng, and W. Zhuang, Chin. J. Chem. Phys. **29**, 445 (2016).

[46] Y.-Y. Liu, Y.-J. Zeng, P.-Z. Jia, X.-H. Cao, X. Jiang, and K.-Q. Chen, J. Phys.: Condens. Matter **30**, 275701 (2018).

[47] J. Hong, C. Lee, J.-S. Park, and J. H. Shim, Phys. Rev. B **93**, 035445 (2016).

[48] W. Shen, D. Zou, G. Nie, and Y. Xu, Chin. Phys. B **26**, 117202 (2017).

[49] Dimple, N. Jena, and A. D. Sarkar, J. Phys.: Condens. Matter **29**, 225501 (2017).

[50] S.-D. Guo, Comput. Mater. Sci. **123**, 8 (2016).

[51] G. Zhang and Y.-W. Zhang, Mech. Mater. **91**, 382 (2015).

[52] H. Y. Lv, W. J. Lu, D. F. Shao, H. Y. Lu, and Y. P. Sun, J. Mater. Chem. C **4**, 4538 (2016).

[53] G. Ding, G. Y. Gao, Z. Huang, W. Zhang, and K. Yao, Nanotechnology **27**, 375703 (2016).

[54] S.-D. Guo and J.-L. Wang, Semicond. Sci. Technol. **31**, 095011 (2016).

[55] Y.-X. Zhen, M. Yang, H. Zhang, G.-S. Fu, J.-L. Wang, S.-F. Wang, and R.-N. Wang, Science Bulletin **62**, 1530 (2017).

[56] D. Qin, X.-J. Ge, G.-q. Ding, G.-y. Gao, and J.-T. Lü, RSC Adv. **7**, 47243 (2017).

[57] H. Y. Lv, W. J. Lu, X. Luo, H. Y. Lu, X. B. Zhu, and Y. P. Sun, arXiv:1608.05464.

[58] G. Kresse and J. Furthmüller, Phys. Rev. B **54**, 11169 (1996).

[59] G. Kresse and D. Joubert, Phys. Rev. B **59**, 1758 (1999).

[60] J. P. Perdew, K. Burke, and M. Ernzerhof, Phys. Rev. Lett. **77**, 3865 (1996).

[61] H. J. Monkhorst and J. D. Pack, Phys. Rev. B **13**, 5188 (1976).

[62] A. V. Krukau, O. A. Vydrov, A. F. Izmaylov, and G. E. Scuseria, J. Chem. Phys. **125**, 224106 (2006).

[63] S. Baroni, S. de Gironcoli, A. Dal Corso, and P. Giannozzi, Rev. Mod. Phys. **73**, 515 (2001).

[64] A. Togo and I. Tanaka, Scr. Mater. **108**, 1 (2015).

[65] G. Henkelman, A. Arnaldsson, and H. Jónsson, Comput. Mater. Sci. **36**, 354 (2006).

[66] W. Callister and D. Rethwisch, *Materials Science and Engineering: An Introduction, 9th Edition: Ninth Edition* (John Wiley and Sons, Incorporated, New York, 2013).

[67] U. Sivan and Y. Imry, Phys. Rev. B **33**, 551 (1986).

[68] K. Esfarjani, M. Zebarjadi, and Y. Kawazoe, Phys. Rev. B **73**, 085406 (2006).

[69] L. G. C. Rego and G. Kirczenow, Phys. Rev. Lett. **81**, 232 (1998).

[70] H. Sevinçli, S. Roche, G. Cuniberti, M. Brandbyge, R. Gutierrez, and L. M. Sandonas, J. Phys.: Condens. Matter **31**, 273003 (2019).

[71] F. A. Rasmussen and K. S. Thygesen, J. Phys. Chem. C **119**, 13169 (2015).

[72] C. Gong, H. Zhang, W. Wang, L. Colombo, R. M. Wallace, and K. Cho, Appl. Phys. Lett. **103**, 053513 (2013).

[73] P. Tsipas, D. Tsoutsou, S. Fragkos, R. Sant, C. Alvarez, H. Okuno, G. Renaud, R. Alcotte, T. Baron, and A. Dimoulas, ACS Nano **12**, 1696 (2018).

[74] S. Aminalragia-Giamini, J. Marquez-Velasco, P. Tsipas, D. Tsoutsou, G. Renaud, and A. Dimoulas, 2D Materials **4**, 015001 (2017).

[75] M. J. Mleczko, C. Zhang, H. R. Lee, H.-H. Kuo, B. Magyari-Köpe, R. G. Moore, Z.-X. Shen, I. R. Fisher, Y. Nishi, and E. Pop, Sci. Adv. **3**, e1700481 (2017).

[76] C. Yan, C. Gong, P. Wangyang, J. Chu, K. Hu, C. Li, X. Wang, X. Du, T. Zhai, Y. Li, and J. Xiong, Adv. Funct. Mater. **28**, 1803305 (2018).

[77] G. Mahan, B. Sales, and J. Sharp, Phys. Today **50**(3), 42 (1997).

[78] J. O. Sofo and G. D. Mahan, Phys. Rev. B **49**, 4565 (1994).

[79] R. P. Chasmar and R. Stratton, J. Electron. Control **7**, 52 (1959).

[80] G. S. Nolas, J. Sharp, and H. J. Goldsmid, *Thermoelectrics: Basic Principles and New Materials Development* (Springer-Verlag, Berlin, Heidelberg, 2001).

[81] A. M. Dehkordi, M. Zebarjadi, J. He, and T. M. Tritt, Mater. Sci. Eng., R **97**, 1 (2015).

[82] B. Singh, C.-H. Hsu, W.-F. Tsai, V. M. Pereira, and H. Lin, Phys. Rev. B **95**, 245136 (2017).

[83] D. L. Duong, M. Burghard, and J. C. Schön, Phys. Rev. B **92**, 245131 (2015).

[84] M. J. Wei, W. J. Lu, R. C. Xiao, H. Y. Lv, P. Tong, W. H. Song, and Y. P. Sun, Phys. Rev. B **96**, 165404 (2017).

[85] C. Chen, B. Singh, H. Lin, and V. M. Pereira, Phys. Rev. Lett. **121**, 226602 (2018).

[86] J.-A. Yan, M. A. D. Cruz, B. Cook, and K. Varga, Sci. Rep. **5**, 16646 (2015).

[87] Z. Zhang, Y. Xie, Y. Ouyang, and Y. Chen, Int. J. Heat Mass Transf. **108**, 417 (2017).

[88] Y. Cai, J. Lan, G. Zhang, and Y.-W. Zhang, Phys. Rev. B **89**, 035438 (2014).

[89] M. Cutler and N. F. Mott, Phys. Rev. **181**, 1336 (1969).

[90] G. D. Guttman, E. Ben-Jacob, and D. J. Bergman, Phys. Rev. B **51**, 17758 (1995).

[91] C. Xu, P. A. Brown, and K. L. Shuford, RSC Adv. **5**, 83876 (2015).

[92] A. Samad, A. Shafique, and Y.-H. Shin, Nanotechnology **28**, 175401 (2017).

[93] See Supplemental Material at http://link.aps.org/supplemental/10.1103/PhysRevB.100.085415 for further figures and tables.